NANO LETTERS

pubs.acs.org/NanoLett Letter

# Mechanical Control of Plasmon Resonances in Ultrathin Metals

Diksha Dadhich, Ruhi Tabassum Hazarika, Sourav Rudra, Prasanna Das, Vijay Bhatia, Ashalatha Indiradevi Kamalasanan Pillai, Magnus Garbrecht, and Bivas Saha*

Cite This: *Nano Lett.* 2026, 26, 6482−6489 Read Online

ACCESS | Metrics & More | Article Recommendations | Supporting Information

**ABSTRACT:** Plasmon resonances arise from the collective oscillations of free electrons in conductive media, enabling strong light−matter interactions. In contrast to semiconductors, the plasmonic response of metals is regarded as intrinsically fixed by their large carrier density and electronic structure and therefore relatively insensitive to external perturbations such as mechanical strain. Here, we show conclusive experimental evidence that plasmon resonances in metals can be actively tuned through strain engineering. Using epitaxial ultrathin titanium nitride (TiN) films, we demonstrate that in-plane tensile strain produces a pronounced blue shift of both unscreened and screened plasmon modes relative to unstrained films of identical thickness, with the magnitude of the shift closely tracking the local strain distribution. First-principles calculations reveal that strain modifies the local defect landscape, which alters the electronic structure, governing the plasmonic response. These results establish strain as an effective control knob for plasmonic properties in metals, enabling mechanically reconfigurable plasmonic and nanophotonic platforms.

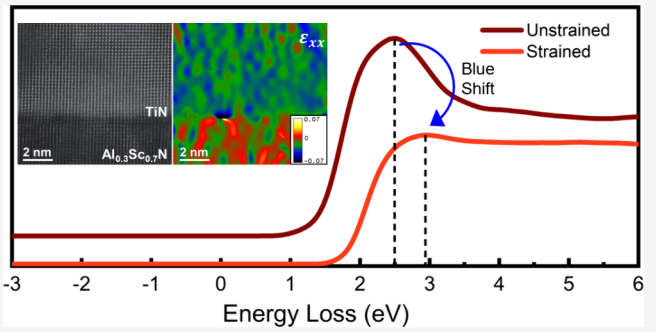


**KEYWORDS:** *Strain engineering, Plasmon resonance, Electron energy loss spectroscopy, Alternative plasmonic materials, Density functional theory*



Plasmon resonances originate from the collective oscillations of free electrons in conductive media, enabling strong confinement and enhancement of electromagnetic fields far below the diffraction limit.[1] These collective excitations support a broad range of nanoscale optical phenomena and technologies, including subwavelength photonic circuitry,[2] ultrasensitive spectroscopy,[3,4] photothermal energy conversion,[5,6] and metasurface-based optical control.[7,8] At the heart of the plasmonic behavior lies the plasma frequency, which, within the Drude description, is generally determined by the free-carrier concentration and effective mass[9] of the material. Consequently, plasmon resonances in metals are generally assumed to occupy fixed spectral positions once the material composition is defined. Although nanostructuring or dielectric engineering can be utilized to tune plasmonic resonances in metals, these approaches primarily modify the electromagnetic environment rather than the intrinsic plasma frequency itself.[10] Consequently, direct modulation of the plasma frequency through mechanical deformation has remained largely unexplored. Achieving external control over plasmon resonances in metals would therefore represent a significant advance, transforming plasmonics from a largely static platform to an active and dynamically tunable one.

Conventional plasmonic platforms are dominated by noble metals such as gold and silver[11] because of their high carrier densities and comparatively low optical losses in the visible and near-infrared spectral ranges. However, despite these advantages, the practical deployment of noble-metal plasmonics at the nanoscale faces persistent limitations. Noble metals exhibit poor thermal and chemical stability, are prone to degradation under high optical or electrical excitation, and remain incompatible with standard complementary metal-oxide semiconductor (CMOS) processing.[12] Moreover, when reduced to ultrathin or nanostructured geometries, noble metals often grow in a discontinuous or island-like manner, resulting in weak intergrain connectivity and enhanced electron scattering at surfaces and grain boundaries. These effects lead to increased optical damping and severely constrain the device performance, scalability, and long-term reliability.[13]

To address these limitations, refractory transition-metal nitrides have emerged as a technologically compelling alternative class of plasmonic materials.[14,12] Among them, titanium nitride (TiN) has attracted particular attention due to its metallic conductivity and plasmonic response[15] comparable to that of gold across the visible-to-near-infrared spectrum,[16] while offering superior mechanical hardness, chemical inert-

Received: March 17, 2026
Revised: April 29, 2026
Accepted: May 6, 2026
Published: May 11, 2026





https://doi.org/10.1021/acs.nanolett.6c01304
*Nano Lett.* 2026, 26, 6482−6489

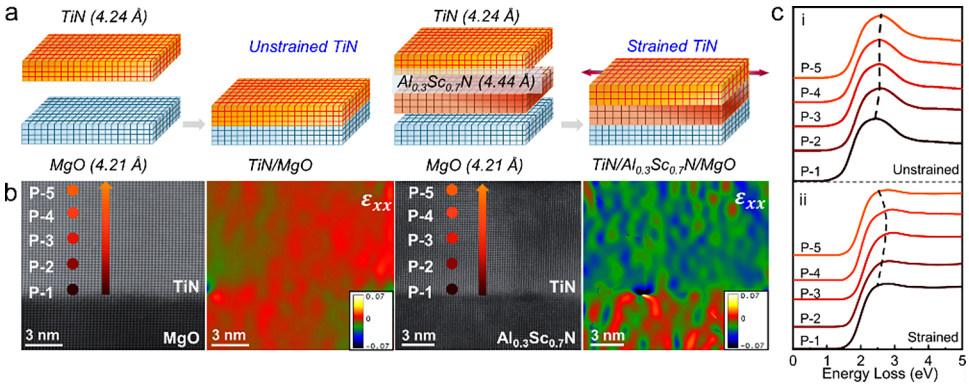


**Figure 1.** Strain engineering of epitaxial TiN heterostructures and its impact on the plasmonic response. (a) Schematics of a (001)-oriented TiN film grown on (001) MgO and on *r*-$Al_{0.3}Sc_{0.7}N$/MgO. The rocksalt crystal structure and closely matched lattice parameters of (001) TiN and (001) MgO result in an essentially strain-free TiN/MgO heterostructure. In contrast, the larger lattice parameter of *r*-$Al_{0.3}Sc_{0.7}N$ imposes biaxial tensile strain on the overgrown (001) TiN film. (b) HAADF-STEM images of nominally unstrained TiN/MgO and strained TiN/*r*-$Al_{0.3}Sc_{0.7}N$/MgO heterostructures, together with GPA maps of the in-plane strain component, $\varepsilon_{xx}$. The TiN/MgO interface is lattice-matched and exhibits negligible strain, whereas TiN grown on *r*-$Al_{0.3}Sc_{0.7}N$ shows a uniform tensile strain of ∼2.35% relative to unstrained TiN. (c) EELS measurements of the screened plasmon excitation acquired at five marked locations in the HAADF-STEM image. Unstrained TiN on MgO exhibits a plasmon energy in the 2.4−2.6 eV range (i), while tensile strain in TiN on *r*-$Al_{0.3}Sc_{0.7}N$ induces a pronounced blue shift to 2.8−3.0 eV (ii).

ness, and thermal stability.[17,18] TiN is corrosion-resistant,[19] maintains structural integrity at elevated temperatures,[20] and is fully compatible with CMOS fabrication workflows,[21,22] making it especially attractive for scalable and durable plasmonic technologies.[23] Importantly, TiN can be grown epitaxially with high crystalline quality,[24] enabling precise control over the film thickness,[25] lattice strain,[26] and defect structure,[27] parameters increasingly recognized as powerful and independent levers for tailoring functional properties in low-dimensional material systems.[28,29]

TiN thin films deposited on single-crystalline substrates exhibit a robust plasmonic response, characterized by an epsilon-near-zero (ENZ) crossover near ∼500 nm and a characteristic gold-like optical appearance.[16] Epitaxial ultrathin TiN films can also be grown on lattice-matched (001) MgO substrates with thicknesses down to just a few monolayers,[30] providing an ideal platform for exploring plasmonic behavior in the extreme confinement regime.[31] Even films as thin as ∼2 nm retain a discernible plasmonic response.[32] However, strong quantum confinement in this ultrathin limit gives rise to pronounced thickness-dependent plasmon resonances, manifested as a systematic red-shift of the resonance energy with decreasing film thickness.[30] In related refractory nitrides such as HfN,[33] where electronic confinement is even stronger, ultrathin films exhibit complete suppression of plasmon resonances at comparable thicknesses. Despite these advances, the influence of lattice strain, an intrinsic and widely tunable parameter in epitaxial thin films, on the plasmonic properties of TiN and other ultrathin metallic systems experimentally remain unexplored.

Strain engineering has been widely and successfully employed in semiconductors to tailor the band structure,[34] carrier transport,[35] and optical transitions,[36] forming the basis of many modern electronic and optoelectronic technologies. In some insulating materials, strain can also directly influence collective electronic excitations such as bulk plasmons through modifications to the electronic structure.[37] In contrast, metals are generally assumed to be largely insensitive to lattice deformation because their high carrier densities and broad electronic bands are thought to render key electronic parameters and hence plasmonic properties effectively strain-invariant. This conventional view, however, neglects the pronounced sensitivity of ultrathin and epitaxial metallic films in which strain can substantially modify the electronic structure, defect landscape, and carrier scattering mechanisms. Moreover, in transition-metal nitrides such as TiN, strain is expected to exert a particularly strong influence on the plasmonic behavior, due to their partially filled d bands and strong electron−lattice coupling, as well as strain-induced modifications to vacancy formation, grain boundaries, and dislocation densities that directly impact plasmon damping and resonance energies.[38] Exploiting strain in such systems thus presents an untapped route to actively modulate plasmonic responses in metals. Here, we demonstrate direct experimental evidence that plasmon resonances in metals can be tuned through mechanical strain.

To unambiguously isolate the influence of lattice strain on the plasmonic properties of TiN, two epitaxial TiN thin films with identical thickness (10 nm) but distinct strain states were prepared. Both films were grown via magnetron sputtering in an ultrahigh-vacuum chamber (base pressure ∼ $1 \times 10^{-9}$ Torr) at 850 °C. One TiN film was deposited directly on a (001) MgO substrate, whose rocksalt crystal structure and closely matched lattice constant (4.21 Å) to that of TiN (4.24 Å) are expected to yield a nearly strain-free epitaxial film (Figure 1a). To introduce controlled tensile strain, a second TiN film is grown on a 65-nm-thick epitaxial *r*-$Al_{0.3}Sc_{0.7}N$ buffer layer deposited on (001) MgO. The $Al_{0.3}Sc_{0.7}N$ layer adopts a rocksalt structure with a larger lattice constant (4.44 Å),[39] corresponding to a theoretical in-plane tensile strain of ∼4.7% in the overlying TiN. The structural quality, strain state, and plasmonic response of both films were systematically characterized using high-resolution X-ray diffraction (HRXRD), high-resolution transmission electron microscopy (HRTEM), and electron energy loss spectroscopy (EELS).

High-angle annular dark-field scanning transmission electron microscopy (HAADF-STEM) imaging of nominally unstrained TiN/MgO and strained ultrathin TiN/*r*-$Al_{0.3}Sc_{0.7}N$/MgO heterostructures (Figure 1b) reveals coherent, layer-by-layer epitaxial growth with a high degree of lattice-plane continuity across the interface. Geometric phase analysis (GPA) strain maps[40] of $\varepsilon_{xx}$ (in-plane) for TiN grown directly on (001) MgO


https://doi.org/10.1021/acs.nanolett.6c01304
Nano Lett. 2026, 26, 6482−6489

show an essentially relaxed film with no measurable in-plane strain. In contrast, TiN deposited on the *r*-$Al_{0.3}Sc_{0.7}N$ buffer layer exhibits a pronounced strain contrast due to the lattice-parameter mismatch between the film and the underlying *r*-$Al_{0.3}Sc_{0.7}N$ buffer layer. The larger lattice constant of *r*-$Al_{0.3}Sc_{0.7}N$ (4.44 Å) imposes biaxial tensile strain on the TiN film. Although the nominal lattice mismatch at the TiN/*r*-$Al_{0.3}Sc_{0.7}N$ interface is ∼4.7%, the experimentally measured in-plane lattice parameter of TiN (4.34 Å) (Figure S1) corresponds to a tensile strain of ∼2.35%, indicating partial strain relaxation.

To correlate the plasmonic response with the local strain state in the TiN films, EELS was performed using a monochromated STEM microscope equipped with a sub-nanometer probe. Zero-loss peak-subtracted and background-corrected EELS spectra[41] were acquired at five distinct locations within the TiN layer, spanning from the substrate/buffer interface to the TiN film surface, and systematically compared to elucidate spatial variations in the plasmon response. Furthermore, the EELS peaks are fitted with a Gaussian function to extract the plasmon resonance energy (Figure S2). The uncertainty in the fitted plasmon peak position, estimated from the Gaussian fitting procedure, was found to be at most 10 meV.

For the unstrained TiN film, the plasmon resonance energy is 2.44 eV at the TiN/MgO interface and increases modestly to 2.53 eV near the middle of the film and to 2.59 eV at the surface. These values are consistent with the ENZ wavelength of ∼520 nm in TiN[42] and correspond to the peak in the energy-loss function discussed below. The plasmon energies measured for the 10-nm TiN film in this work are also in good agreement with previous reports on magnetron-sputtered thick TiN films, which exhibit plasmon resonances in the 2.3−2.8 eV spectral range.[43,44] Notably, in contrast to the clearly resolved screened and unscreened plasmon resonance components observed in relatively thicker films, the 10-nm TiN film studied here exhibits a predominantly interface-like plasmonic response.

Compared to the relaxed film, the strained TiN film displays a substantially higher plasmon resonance energy of 2.81 eV near the TiN/*r*-$Al_{0.3}Sc_{0.7}N$ interface, which further increases to 2.97 eV toward the middle of the layer before decreasing slightly at larger thicknesses. Overall, the strained TiN film exhibits a pronounced blue shift of approximately 0.30−0.45 eV relative to the unstrained TiN, particularly close to the film/buffer interface, where the tensile strain is maximal (Table 1). Because strain is progressively relaxed with increasing film thickness, the observed reduction in the plasmon resonance energy at greater depths is attributed to partial strain relaxation within the TiN layer, as discussed below. Collectively, these findings establish strain as an effective control parameter for modulating the plasmon resonance energy in TiN, overturning the conventional view of a spectrally fixed response.

**Table 1. Gaussian-Fitted Peak Positions (eV) of Screened Plasmon Resonance Energies in TiN at Each of the Marked Regions in Figure 1[a]**

| marked point | TiN/MgO | TiN/$Al_{0.3}Sc_{0.7}N$/MgO |
|---|---|---|
| P-1 | 2.45 | 2.81 |
| P-2 | 2.58 | 2.87 |
| P-3 | 2.53 | 2.98 |
| P-4 | 2.56 | 2.93 |
| P-5 | 2.59 | 2.82 |

[a]The peak positions have an estimated uncertainty of about 10 meV.

To further establish the structural origin of the strain state and its correlation with the plasmonic response, low-magnification HAADF-STEM imaging was performed over extended regions of the heterostructure. As shown in Figure 2a, both the *r*-$Al_{0.3}Sc_{0.7}N$ buffer layer and the TiN film are laterally homogeneous and uniformly thick, with atomically sharp and well-defined *r*-$Al_{0.3}Sc_{0.7}N$/MgO and TiN/*r*-$Al_{0.3}Sc_{0.7}N$ interfaces. The corresponding selected-area electron diffraction (SAED) pattern confirms the cubic rocksalt structure and the epitaxial nature of the TiN layer. GPA performed over a large field of view reveals the spatial distribution of strain across the entire TiN/*r*-$Al_{0.3}Sc_{0.7}N$/MgO interface, corroborating the tensile strain imposed on TiN by the larger lattice parameter of the underlying *r*-$Al_{0.3}Sc_{0.7}N$ buffer layer. Because of the strong Z-contrast in HAADF-STEM, the TiN layer appears brighter than the lighter *r*-$Al_{0.3}Sc_{0.7}N$, enabling clear delineation of the individual layers. Energy-dispersive X-ray spectroscopy (EDS) elemental maps (Figure 2d) further demonstrate a uniform spatial distribution of Ti, N, Al, and Sc with a small and comparable oxygen impurity level in both the strained and unstrained films. This equivalence in the oxygen concentration rules out oxygen-impurity-driven variations in the carrier density as the origin of the observed plasmon energy shifts, reinforcing strain-induced increased carrier density due to donor nitrogen vacancy formation as the dominant mechanism.

In addition to the screened plasmon frequency, the unscreened plasmon excitation also exhibits a clear blue shift in the strained TiN film relative to the fully relaxed TiN grown directly on MgO (Figure 2e). Quantitative analysis of the EELS spectra reveals that the unscreened plasmon energy at the TiN/MgO interface is located at 21.33 eV, whereas the corresponding excitation at the TiN/*r*-$Al_{0.3}Sc_{0.7}N$ interface occurs at a higher energy of 23.22 eV (Table S1). With an increase in the distance from the interface toward the TiN surface, the unscreened plasmon energy rises in both heterostructures. However, across the entire depth profile, the strained TiN consistently exhibits a plasmon energy that is higher than that of its strain-free counterpart. This systematic and spatially resolved blue shift of the unscreened plasmon resonance energy further substantiates the conclusion that tensile strain in TiN directly modifies its collective electronic response, in agreement with the trends observed for the screened plasmon resonance.

To gain information from a wide sample area, the structural properties of ultrathin TiN films were investigated using high-resolution X-ray diffraction (HRXRD). Symmetric $2\theta-\omega$ measurements (Figure 3a) confirm that TiN grows with a (002) out-of-plane orientation on both substrates, establishing epitaxial and nominally single-crystalline growth in both the strain-free and strained heterostructures. For TiN deposited directly on (001) MgO, a well-defined TiN (002) reflection is observed at 42.71°, corresponding to an out-of-plane lattice parameter of 4.23 Å. Pronounced thickness fringes indicative of high crystalline quality and atomically sharp interfaces are also observed. In contrast, for TiN grown on the *r*-$Al_{0.3}Sc_{0.7}N$ buffer layer, the TiN (002) reflection overlaps with the MgO substrate peak near 42.4°, accompanied by weak interference fringes. This overlap reflects out-of-plane lattice compression arising from an in-plane tensile strain, which drives the TiN


https://doi.org/10.1021/acs.nanolett.6c01304
Nano Lett. 2026, 26, 6482−6489

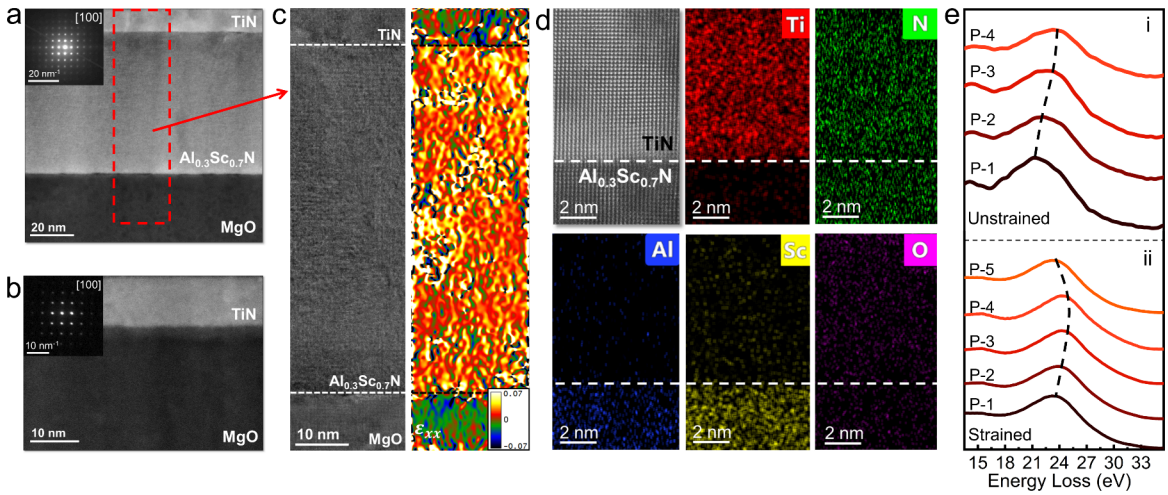


**Figure 2.** Structural, chemical, and plasmonic characterization of strained and unstrained TiN heterostructures. (a) Low-magnification HAADF-STEM image of a homogeneous and uniform TiN/*r*-$Al_{0.3}Sc_{0.7}N$ heterostructure deposited on a (001) MgO substrate. The *r*-$Al_{0.3}Sc_{0.7}N$ buffer layer is introduced to impose lattice mismatch and induce strain in the overlying TiN film. The inset shows a SAED pattern acquired along the [001] zone axis, confirming cubic epitaxial growth of the heterostructure. (b) HAADF-STEM overview image of TiN grown directly on (001) MgO, demonstrating homogeneous, strain-free epitaxial growth. (c) GPA map of the in-plane strain component, $\varepsilon_{xx}$, across the entire TiN/*r*-$Al_{0.3}Sc_{0.7}N$/MgO stack, highlighting the larger lattice parameter of the *r*-$Al_{0.3}Sc_{0.7}N$ layer and the resulting tensile strain in the TiN film. (d) High-resolution HAADF-STEM image of TiN on *r*-$Al_{0.3}Sc_{0.7}N$, together with EDS elemental maps of Ti, N, Al, Sc, and O, demonstrating chemically uniform and well-defined interfaces. (e) Comparison of EELS spectra acquired at the five marked locations (Figure 1b), corresponding to the unscreened plasmon excitation. The strained TiN film (ii) exhibits a pronounced blue shift in the unscreened plasmon energy relative to strain-free TiN (i), mirroring the trend observed for the screened plasmon resonance.

lattice parameter closer to that of MgO, consistent with coherent or partially coherent epitaxial constraint. The epitaxial relationship is further confirmed by pole-figure measurements (Figure 3b). The asymmetric TiN (111) pole figure for TiN/*r*-$Al_{0.3}Sc_{0.7}N$ exhibits four symmetrically spaced diffraction maxima at $\chi \approx 54.7°$, characteristic of 4-fold cubic epitaxy. An analogous 4-fold symmetry is also observed for the *r*-$Al_{0.3}Sc_{0.7}N$ buffer layer (Figure S5), confirming that TiN inherits the crystallographic symmetry of the underlying epitaxial template.

Reciprocal space maps (RSMs) around the asymmetric (113) reflection provide further insight into the strain state of the films (Figure 3c,d). For strain-free TiN/MgO (Figure 3c), the TiN and MgO diffraction peaks are vertically aligned along $Q_x$, confirming in-plane lattice matching, while a slight elongation along $Q_z$ reflects the small difference in the out-of-plane lattice parameters. In contrast, the RSM of the TiN/*r*-$Al_{0.3}Sc_{0.7}N$/MgO heterostructure (Figure 3d) reveals two well-separated peaks corresponding to MgO and the *r*-$Al_{0.3}Sc_{0.7}N$ buffer layer, demonstrating their in-plane lattice mismatch and confirming that the buffer layer is fully relaxed at a thickness of ∼65 nm. The TiN diffraction signal coincides with the MgO peak and exhibits noticeable broadening, indicating that the ultrathin TiN film experiences tensile strain while remaining laterally constrained by the substrate. Because the TiN diffraction peak overlaps with that of MgO in reciprocal space, ultrathin film thickness, and the close similarity of lattice parameters, XRD alone cannot unambiguously quantify the strain state within the TiN layer. Consequently, direct real-space strain mapping using HAADF-STEM and GPA (Figure 2) has been performed to resolve the local strain distribution in TiN, providing the basis for correlating epitaxial strain with the observed plasmonic response.

To elucidate the plasmonic response of ultrathin TiN and to confirm that the $Al_{0.3}Sc_{0.7}N$ buffer layer does not exhibit any plasmonic signature in the visible spectral range, optical characterization of the films is performed using spectroscopic ellipsometry, complemented by first-principles density functional theory (DFT) calculations. The ellipsometry-derived real and imaginary components of the dielectric permittivity reveal that the strain-free 10 nm TiN film exhibits an ENZ crossover at ∼520 nm, which closely matches the ENZ wavelength of ∼480 nm observed in a thicker TiN film grown under identical conditions. This slight red shift of the ENZ wavelength[45,32] in the ultrathin TiN layer is consistent with its marginally reduced carrier concentration relative to the thick TiN film. As shown in Figure 4a, the thicker TiN film displays a modestly larger real part of the dielectric permittivity ($\varepsilon'$), reflecting a stronger free-electron Drude response arising from its higher carrier density. Correspondingly, the optical losses, represented by the imaginary part of the dielectric permittivity ($\varepsilon''$), are slightly larger in the thicker film over most of the measured spectral range. Notably, in the visible regime, the 10-nm TiN film exhibits a somewhat enhanced optical loss, which is attributed to increased surface and interface scattering in the ultrathin limit.

In contrast, ellipsometry measurements of the *r*-$Al_{0.3}Sc_{0.7}N$ buffer layer show that $\varepsilon'$ remains positive across the ultraviolet, visible, and near-infrared spectral ranges, confirming its dielectric character.[39] The corresponding $\varepsilon''$ spectrum exhibits a peak associated with interband transitions and remains relatively low at longer wavelengths. Due to the large number of fitting parameters in the TiN/$Al_{0.3}Sc_{0.7}N$/MgO multilayer heterostructure, reliable extraction of the dielectric function of the strained TiN layer deposited on the $Al_{0.3}Sc_{0.7}N$ buffer layer was not possible. Nevertheless, the energy-loss function, $\mathrm{Im}[-1/\varepsilon(\omega)]$, calculated from the ellipsometry-derived dielectric permittivity[46] of both the thick and ultrathin TiN films shows excellent agreement with the experimentally measured EELS spectra, as illustrated in Figure 4c. Compared


https://doi.org/10.1021/acs.nanolett.6c01304
Nano Lett. 2026, 26, 6482−6489

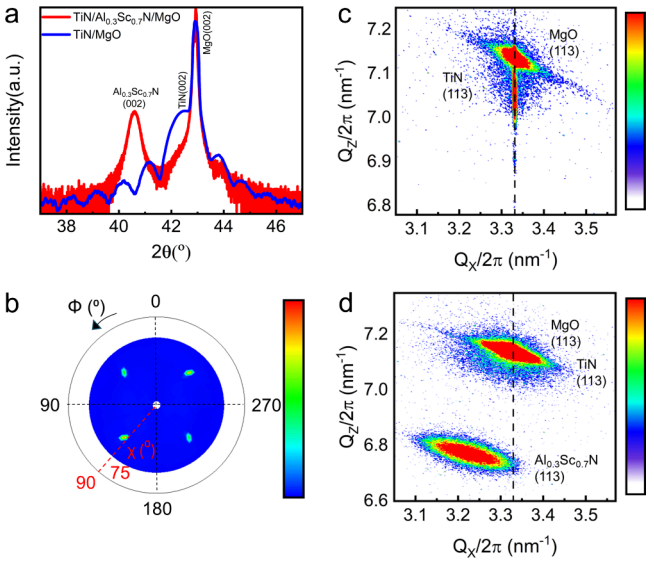


**Figure 3.** XRD analysis of strain-free and strained TiN heterostructures. (a) Symmetric $2\theta-\omega$ XRD patterns of 10 nm TiN films deposited directly on (001) MgO (strain-free, blue) and on an *r*-$Al_{0.3}Sc_{0.7}N$ buffer layer on MgO (strained, red), showing (002)-oriented TiN growth. Pronounced thickness fringes in the TiN/MgO XRD pattern indicate high crystalline quality and atomically sharp interfaces. For TiN deposited on *r*-$Al_{0.3}Sc_{0.7}N$, the TiN (002) peak overlaps with the MgO substrate peak, reflecting out-of-plane lattice compression induced by in-plane tensile strain, which drives the TiN lattice parameter closer to that of MgO. (b) Pole figure measured around the asymmetric TiN(111) reflection for TiN/*r*-$Al_{0.3}Sc_{0.7}N$, showing four symmetrically spaced diffraction maxima characteristic of 4-fold cubic epitaxy. (c) RSM around the asymmetric (113) reflection for strain-free TiN/MgO, where the vertical alignment of the TiN and MgO peaks along $Q_x$ confirms in-plane lattice matching. The slight elongation along $Q_z$ reflects the small difference in the out-of-plane lattice parameters. (d) RSM around the (113) reflection for strained TiN/*r*-$Al_{0.3}Sc_{0.7}N$/MgO, revealing two well-separated peaks corresponding to MgO and *r*-$Al_{0.3}Sc_{0.7}N$, indicative of their in-plane lattice mismatch. The TiN peak coincides with MgO along $Q_x$, while its broadening reflects the presence of tensile strain within the TiN layer.

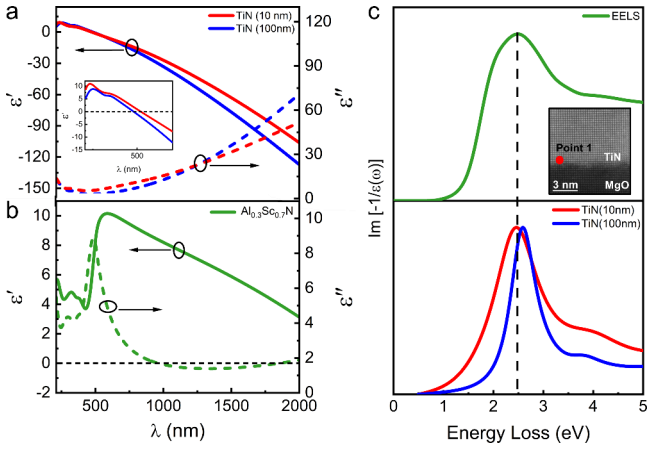


**Figure 4.** Optical dielectric response and energy-loss characteristics of TiN and *r*-$Al_{0.3}Sc_{0.7}N$ thin films. (a) Real ($\varepsilon'$) and imaginary ($\varepsilon''$) parts of the dielectric permittivity of 10-nm (red) and 100-nm (blue) TiN films grown on (001) MgO substrates. Both films exhibit a plasmonic response with an ENZ crossover near ∼500 nm (inset). Compared to the thicker film, the 10-nm TiN layer shows enhanced optical losses in the visible spectral range. (b) Real ($\varepsilon'$) and imaginary ($\varepsilon''$) components of the dielectric permittivity of rocksalt *r*-$Al_{0.3}Sc_{0.7}N$ grown on (001) MgO, confirming its dielectric behavior across the measured spectral range. (c) Energy-loss function, $\mathrm{Im}[-1/\varepsilon(\omega)]$, calculated from the ellipsometry-derived permittivity of TiN films and compared with experimentally measured EELS spectra at the TiN/substrate interface (inset), demonstrating close agreement between the optical and electron-based probes of the plasmon response.

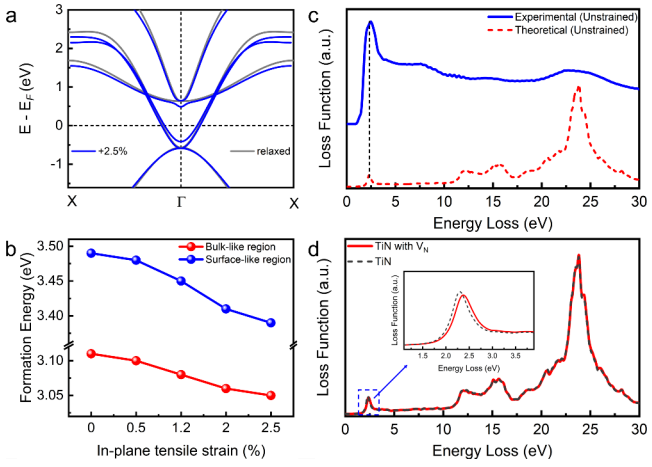


**Figure 5.** Calculated electronic structure, defect formation energy, and loss function. (a) Electronic band structure for relaxed (gray) and strained (blue) TiN along the in-plane direction. The electronic dispersion does not exhibit a significant change from strain. (b) Calculated nitrogen vacancy formation energy $E_f(V_N)$ for TiN with different amounts of in-plane tensile strain, at the middle of the slab layer (red) and at the surface (blue). With strain in the layer, $V_N$ formation becomes more feasible. (c) Comparison between theoretically calculated and experimentally determined EELS for an unstrained TiN. (d) Computationally calculated EELS for TiN incorporating additional negative charge (solid red) and compared with the calculated EELS of pristine TiN (dashed gray). Consistent with the experimental observations, TiN with $V_N$ exhibits a higher plasma resonance peak (inset) energy.

to the thicker film, the 10-nm TiN layer exhibits a slightly broader loss-function peak, consistent with the experimentally observed EELS line shape. Such broadening reflects the enhanced optical damping in the ultrathin film, arising from increased electron scattering at surfaces and interfaces.[30]

Since both the strain-free and strained 10-nm TiN films are far outside the strong quantum confinement regime,[32] their plasmonic response can be adequately described using semiclassical Drude theory. Within this model, the plasma frequency $\omega_p$ is governed by the free-carrier concentration ($N$) and the carrier effective mass ($m^*$). Therefore, to elucidate the microscopic origin of the strain-induced blue shift of the plasmon resonance, first-principles DFT calculations, as implemented in Quantum Espresso, are performed to examine the strain dependence of the electronic band structure, carrier effective mass, and defect formation energetics in TiN. As shown in Figure 5a, ∼2.5% biaxial tensile strain leads to minimal changes in the electronic structure[47] of TiN near the Fermi level. In particular, tensile strain shows no significant changes in the band curvature, resulting in similar effective masses of the carriers (Figure S8).

Although the carrier effective mass remains essentially unchanged under tensile strain, the free-carrier concentration in TiN can vary substantially due to strain-induced



https://doi.org/10.1021/acs.nanolett.6c01304
Nano Lett. 2026, 26, 6482−6489

modifications of defect energetics. To clarify this mechanism, the formation energy of nitrogen vacancy $E_f(V_N)$ values under different levels of in-plane tensile strain are calculated,[48] considering both bulk-like and surface-like regions (Figure 5b) in a vertical slab mimicking the ultrathin layer (Figure S7). The calculations reveal a systematic reduction in $E_f(V_N)$ with increasing tensile strain, indicating that $V_N$s become energetically more favorable in tensile-strained TiN. Because $V_N$s act as electron donors in TiN,[49] their enhanced formation under tensile strain leads to an increased electron concentration, which, in turn, raises the plasma frequency within the Drude framework.

Importantly, the calculations also explain the experimentally observed depth dependence of the plasmon energy. The reduction in $E_f(V_N)$ is more pronounced in the bulk region than at the surface, resulting in a higher $V_N$ and electron concentration and, consequently, a larger plasmon resonance energy away from the surface. This trend is fully consistent with the spatially resolved EELS measurements shown in Figures 1c and 2e, as well as with earlier theoretical predictions.[43] Collectively, these results establish strain-driven defect engineering as the microscopic origin of the observed blue shift in the plasmon resonance of TiN.

To further validate our theoretical framework, a direct comparison between the calculated energy-loss spectrum and the experimentally measured EELS data for the unstrained TiN film[50] (Figure 5c) is made. The theoretically derived screened plasmon energy shows excellent agreement with the experimental value, confirming the reliability of the computational approach in capturing the essential electronic response of TiN. Additionally, the EELS data (Figure 5d) for unstrained TiN is simulated by incorporating an additional negative charge corresponding to the experimental excess electron concentration of $\sim 7.4 \times 10^{21}$ $cm^{-3}$, arising from $V_N$s in the strained film. Compared to pristine unstrained TiN, the calculated spectrum exhibits a blue shift, further confirming the influence of the additional charge introduced by $V_N$ formation.

Taken together, these findings establish a clear microscopic mechanism for the strain-induced enhancement of the plasmon resonance energy in ultrathin TiN. Epitaxial tensile strain increases the plasmon resonance energy primarily through strain-stabilized donor-like $V_N$s that elevate the free-electron concentration in the strained film, while the carrier effective mass remains largely unchanged. This combined insight provides a coherent and quantitatively supported explanation for the experimentally observed blue shift of the plasmon resonance energy in the strained ultrathin film.

In summary, we demonstrate that plasmon resonances in epitaxial TiN can be actively tuned through lattice strain, challenging the long-standing assumption that metallic plasmon frequencies are spectrally fixed by the composition alone. By comparing strain-free and biaxially tensile-strained 10-nm TiN films, we observe a pronounced and spatially resolved blue shift of both screened and unscreened plasmon resonances under tensile strain. Correlative EELS, ellipsometry, and first-principles calculations reveal that tensile strain stabilizes donor-like $V_N$s, thereby increasing the free-electron concentration and plasma frequency with minimal impact on the carrier effective mass. These findings establish strain-driven defect engineering as a powerful and previously underexplored route for modulating collective electronic excitations in refractory plasmonic metals. More broadly, our work introduces epitaxial strain as a viable design parameter for actively tuning plasmonic responses in transition-metal nitrides, opening new opportunities for mechanically programmable and CMOS-compatible plasmonic devices.

## ■ ASSOCIATED CONTENT

### Data Availability Statement

The data that support the findings of this study are available from the corresponding author upon reasonable request.

### Supporting Information

The Supporting Information is available free of charge at https://pubs.acs.org/doi/10.1021/acs.nanolett.6c01304.

Detailed experimental and computational methods, including the growth process, characterization methods, lattice fringe plot, raw EELS data, Gaussian-fitted EELS data, a table containing unscreened plasmon energy values, a pole figure of $r$-$Al_{0.3}Sc_{0.7}N$, reflectance spectra for 10 and 100 nm samples, and theoretical methods (PDF)

## ■ AUTHOR INFORMATION


### Corresponding Author

**Bivas Saha** − *Chemistry and Physics of Materials Unit, International Centre for Materials Science (ICMS), and School of Advanced Materials and Sheikh Saqr Laboratory (SSL), Jawaharlal Nehru Centre for Advanced Scientific Research (JNCASR), Bangalore 560064, India;* orcid.org/0000-0002-0837-1506; Email: bsaha@jncasr.ac.in, bivas.mat@gmail.com

### Authors

**Diksha Dadhich** − *Chemistry and Physics of Materials Unit and International Centre for Materials Science (ICMS), Jawaharlal Nehru Centre for Advanced Scientific Research (JNCASR), Bangalore 560064, India*

**Ruhi Tabassum Hazarika** − *Chemistry and Physics of Materials Unit and International Centre for Materials Science (ICMS), Jawaharlal Nehru Centre for Advanced Scientific Research (JNCASR), Bangalore 560064, India*

**Sourav Rudra** − *Chemistry and Physics of Materials Unit and International Centre for Materials Science (ICMS), Jawaharlal Nehru Centre for Advanced Scientific Research (JNCASR), Bangalore 560064, India*

**Prasanna Das** − *Chemistry and Physics of Materials Unit and International Centre for Materials Science (ICMS), Jawaharlal Nehru Centre for Advanced Scientific Research (JNCASR), Bangalore 560064, India;* orcid.org/0000-0003-1138-7557

**Vijay Bhatia** − *Sydney Microscopy and Microanalysis, The University of Sydney, Camperdown, New South Wales 2006, Australia;* orcid.org/0000-0003-1804-4231

**Ashalatha Indiradevi Kamalasanan Pillai** − *Sydney Microscopy and Microanalysis, The University of Sydney, Camperdown, New South Wales 2006, Australia*

**Magnus Garbrecht** − *Sydney Microscopy and Microanalysis, The University of Sydney, Camperdown, New South Wales 2006, Australia;* orcid.org/0000-0002-1852-5580

Complete contact information is available at: https://pubs.acs.org/10.1021/acs.nanolett.6c01304




https://doi.org/10.1021/acs.nanolett.6c01304
Nano Lett. 2026, 26, 6482−6489

## Author Contributions

D.D. and B.S. conceived this project. D.D. deposited thin films. R.T.H., S.R., and B.S. performed theoretical calculations. P.D. and D.D. performed optical characterization. D.D. performed structural and electrical characterization and EELS data plotting with analysis. V.B. and A.I.K.P. performed TEM sample preparation, and M.G. performed TEM imaging, EELS, and EDS mapping. D.D. and M.G. performed GPA strain mapping. All authors discussed and contributed to the preparation of the manuscript.

## Notes

The authors declare no competing financial interest.

## ■ ACKNOWLEDGMENTS

D.D. and B.S. acknowledge support of the ICMS and SSL in JNCASR. B.S. acknowledges the Anusandhan National Research Foundation (ANRF) in India for Core Research Grant CRG/2023/007061 for financial support. S.R. and P.D. thank the Council of Scientific and Industrial Research for fellowships. D.D. thanks JNCASR for a fellowship. R.T.H. thanks ANRF for a fellowship. S.R. and B.S. sincerely acknowledge the support and resources provided by PARAM Yukti Facility under the National Supercomputing Mission, Government of India, at JNCASR, Bangalore. M.G., V.B., and A.I.K.P. acknowledge the Sydney Microscopy and Microanalysis facilities at the University of Sydney. D.D. acknowledges Sudip Mahato for providing help with GATAN DigitalMicrograph software. D.D. acknowledges Renuka Manish Karanje for helping with the HRXRD RSM and pole figure. D.D. acknowledges Debmalya Mukhopadhyay's help in performing optical characterizations. D.D. acknowledges Subhajit Manna for helping with GPA strain mapping.

## ■ REFERENCES

(1) Polman, A.; Atwater, H. A. Plasmonics: Optics at the Nanoscale. *Mater. Today* **2005**, *8* (1), 56.
(2) Vertchenko, L.; Akopian, N.; Lavrinenko, A. V. Epsilon-Near-Zero Grids for On-Chip Quantum Networks. *Sci. Rep.* **2019**, *9* (1), 6053.
(3) Yin, J.; Zang, Y.; Yue, C.; Wu, Z.; Wu, S.; Li, J.; Wu, Z. Ag Nanoparticle/ZnO Hollow Nanosphere Arrays: Large Scale Synthesis and Surface Plasmon Resonance Effect Induced Raman Scattering Enhancement. *J. Mater. Chem.* **2012**, *22* (16), 7902.
(4) Li, R.; Liu, K.; Pan, S.; Ding, J. H. Localized Surface Plasmon Resonance of Single Silver Nano-Hemisphere. *Adv. Mater. Res.* **2013**, *818*, 137−140.
(5) Bubnov, A. A.; Syui, A. V.; Popov, A. A.; Tikhonovskii, G. V.; Pokryshkin, N. S.; Timoshenko, V. Y. Comparative Study of Photothermal Conversion Efficiency in Aqueous Suspensions of Silicon and Titanium Nitride Nanoparticles for Biomedical Applications. *Phys. At. Nucl.* **2023**, *86* (12), 2743−2747.
(6) Chirumamilla, M.; Chirumamilla, A.; Yang, Y.; Roberts, A. S.; Kristensen, P. K.; Chaudhuri, K.; Boltasseva, A.; Sutherland, D. S.; Bozhevolnyi, S. I.; Pedersen, K. Large-Area Ultrabroadband Absorber for Solar Thermophotovoltaics Based on 3D Titanium Nitride Nanopillars. *Adv. Opt. Mater.* **2017**, *5* (22), 1−8.
(7) Beliaev, L. Y.; Shkondin, E.; Lavrinenko, A. V.; Takayama, O. Titanium Nitride Nanotrench Metasurfaces for Mid-Infrared Chemical Sensing. *ACS Appl. Opt. Mater.* **2024**, *2* (1), 88−96.
(8) Huo, D.; Ma, X.; Su, H.; Wang, C.; Zhao, H. Broadband Absorption Based on Thin Refractory Titanium Nitride Patterned Film Metasurface. *Nanomaterials* **2021**, *11* (5), 1092.
(9) Li, H. Y.; Zhou, S. M.; Li, J.; Chen, Y. L.; Wang, S. Y.; Shen, Z. C.; Chen, L. Y.; Liu, H.; Zhang, X. X. Analysis of the Drude Model in Metallic Films. *Appl. Opt.* **2001**, *40* (34), 6307.
(10) Brongersma, M. L.; Halas, N. J.; Nordlander, P. Plasmon-Induced Hot Carrier Science and Technology. *Nat. Nanotechnol.* **2015**, *10* (1), 25−34.
(11) Atwater, H. A. The Promise of Plasmonics. *Sci. Am.* **2007**, *296* (4), 56−62.
(12) Naik, G. V.; Shalaev, V. M.; Boltasseva, A. Alternative Plasmonic Materials: Beyond Gold and Silver. *Adv. Mater.* **2013**, *25* (24), 3264−3294.
(13) West, P. R.; Ishii, S.; Naik, G. V.; Emani, N. K.; Shalaev, V. M.; Boltasseva, A. Searching for Better Plasmonic Materials. *Laser Photon. Rev.* **2010**, *4* (6), 795−808.
(14) Bi, J.; Zhang, R.; Yao, X.; Cao, Y. The Rise of Refractory Transition-Metal Nitride Films for Advanced Electronics and Plasmonics. *Adv. Mater. Interfaces* **2025**, *12* (12), 1−19.
(15) Patsalas, P.; Kalfagiannis, N.; Kassavetis, S. Optical Properties and Plasmonic Performance of Titanium Nitride. *Materials (Basel).* **2015**, *8* (6), 3128−3154.
(16) Guo, W.-P.; Mishra, R.; Cheng, C.-W.; Wu, B.-H.; Chen, L.-J.; Lin, M.-T.; Gwo, S. Titanium Nitride Epitaxial Films as a Plasmonic Material Platform: Alternative to Gold. *ACS Photonics* **2019**, *6* (8), 1848−1854.
(17) Patsalas, P.; Logothetidis, S. Optical, Electronic, and Transport Properties of Nanocrystalline Titanium Nitride Thin Films. *J. Appl. Phys.* **2001**, *90* (9), 4725−4734.
(18) Bower, R.; McPolin, C. P. T.; Krasavin, A. V.; Zayats, A. V.; Petrov, P. K. Temperature Stability of Individual Plasmonic Au and TiN Nanodiscs. *Opt. Mater. Express* **2022**, *12* (9), 3471.
(19) Datta, S.; Das, M.; Balla, V. K.; Bodhak, S.; Murugesan, V. K. Mechanical, Wear, Corrosion and Biological Properties of Arc Deposited Titanium Nitride Coatings. *Surf. Coat. Technol.* **2018**, *344*, 214−222.
(20) Babinova, R. V.; Smirnov, V. V.; Useenov, A. S.; Kravchuk, K. S.; Gladkikh, E. V.; Shapovalov, V. I.; Mylnikov, I. L. Mechanical Properties of Titanium Nitride Films Obtained by Reactively Sputtering with Hot Target. *J. Phys. Conf. Ser.* **2017**, *872* (1), No. 012035.
(21) Briggs, J. A.; Naik, G. V.; Petach, T. A.; Baum, B. K.; Goldhaber-Gordon, D.; Dionne, J. A. Fully CMOS-Compatible Titanium Nitride Nanoantennas. *Appl. Phys. Lett.* **2016**, *108* (5). DOI: 10.1063/1.4941413.
(22) Nardi, A.; Turchetti, M.; Britton, W. A.; Chen, Y.; Yang, Y.; Dal Negro, L.; Berggren, K. K.; Keathley, P. D. Nanoscale Refractory Doped Titanium Nitride Field Emitters. *Nanotechnology* **2021**, *32* (31), 315208.
(23) Gui, L.; Bagheri, S.; Strohfeldt, N.; Hentschel, M.; Zgrabik, C. M.; Metzger, B.; Linnenbank, H.; Hu, E. L.; Giessen, H. Nonlinear Refractory Plasmonics with Titanium Nitride Nanoantennas. *Nano Lett.* **2016**, *16* (9), 5708−5713.
(24) Zgrabik, C. M.; Hu, E. L. Optimization of Sputtered Titanium Nitride as a Tunable Metal for Plasmonic Applications. *Opt. Mater. Express* **2015**, *5* (12), 2786.
(25) Saha, S.; Ozlu, M. G.; Chowdhury, S. N.; Diroll, B. T.; Schaller, R. D.; Kildishev, A.; Boltasseva, A.; Shalaev, V. M. Tailoring the Thickness-Dependent Optical Properties of Conducting Nitrides and Oxides for Epsilon-Near-Zero-Enhanced Photonic Applications. *Adv. Mater.* **2023**, *35* (34), 1−18.
(26) Smith, H. A.; Elhamri, S.; Eyink, K. G.; Biegler, Z. J.; Adams, R. L.; Mahalingam, K.; Back, T. C.; Urbas, A. M.; Reed, A. N. Investigation of Strain and Stoichiometry of Epitaxial Titanium Nitride on Sapphire. *Thin Solid Films* **2020**, *697*, 137832.
(27) Zhang, R.; Ma, Q.-Y.; Liu, H.; Sun, T.-Y.; Bi, J.; Song, Y.; Peng, S.; Liang, L.; Gao, J.; Cao, H.; Huang, L.-F.; Cao, Y. Crystal Orientation-Dependent Oxidation of Epitaxial TiN Films with Tunable Plasmonics. *ACS Photonics* **2021**, *8* (3), 847−856.
(28) Wang, Y.; Capretti, A.; Dal Negro, L. Wide Tuning of the Optical and Structural Properties of Alternative Plasmonic Materials. *Opt. Mater. Express* **2015**, *5* (11), 2415.
(29) Braic, L.; Vasilantonakis, N.; Mihai, A.; Villar Garcia, I. J.; Fearn, S.; Zou, B.; Alford, N. M.; Doiron, B.; Oulton, R. F.; Maier, S.


https://doi.org/10.1021/acs.nanolett.6c01304
Nano Lett. 2026, 26, 6482−6489

A.; Zayats, A. V.; Petrov, P. K. Titanium Oxynitride Thin Films with Tunable Double Epsilon-Near-Zero Behavior for Nanophotonic Applications. *ACS Appl. Mater. Interfaces* **2017**, *9* (35), 29857−29862.
(30) Shah, D.; Reddy, H.; Kinsey, N.; Shalaev, V. M.; Boltasseva, A. Optical Properties of Plasmonic Ultrathin TiN Films. *Adv. Opt. Mater.* **2017**, *5* (13), 1−5.
(31) Huang, J.; Zhang, D.; Wang, H. Epitaxial TiN/MgO Multilayers with Ultrathin TiN and MgO Layers as Hyperbolic Metamaterials in Visible Region. *Mater. Today Phys.* **2021**, *16*, 100316.
(32) Shah, D.; Yang, M.; Kudyshev, Z.; Xu, X.; Shalaev, V. M.; Bondarev, I. V.; Boltasseva, A. Thickness-Dependent Drude Plasma Frequency in Transdimensional Plasmonic TiN. *Nano Lett.* **2022**, *22* (12), 4622−4629.
(33) Das, P.; Rudra, S.; Rao, D.; Banerjee, S.; Indiradevi, A.; Garbrecht, M.; Boltasseva, A.; Bondarev, I. V.; Shalaev, V. M.; Saha, B. Electron Confinement−Induced Plasmonic Breakdown in Metals. *Sci. Adv.* **2024**, *10* (47), 1−8.
(34) Shukla, N.; Rudra, S.; Karanje, R.; Mukhopadhyay, D.; Das, P.; Biswas, B.; Baral, M.; Gupta, M.; Saha, B. Strain-Induced Valence Band Splitting Enabling Above-Bandgap Exciton Luminescence in Epitaxial Mg 3 N 2 Thin Films. *Chem. Mater.* **2024**, *36* (11), 5563−5573.
(35) Rudra, S.; Rao, D.; Poncé, S.; Saha, B. Reversal of Band-Ordering Leads to High Hole Mobility in Strained p -Type Scandium Nitride. *Nano Lett.* **2023**, *23* (17), 8211−8217.
(36) le Febvrier, A.; Honnali, S. K.; Poterie, C.; Fernandes, T. V.; Frost, R.; Rogoz, V.; Magnuson, M.; Giovannelli, F.; Leitão, J. P.; Barbot, J. F.; Eklund, P. Strain Engineering of ScN Thin Films and Its Effect on Optical, Electrical, and Thermoelectric Properties. *J. Mater. Chem. A* **2026**, *14* (3), 1666−1680.
(37) Palisaitis, J.; Hsiao, C.-L.; Junaid, M.; Birch, J.; Hultman, L.; Persson, P. O. Å. Effect of Strain on Low-Loss Electron Energy Loss Spectra of Group-III Nitrides. *Phys. Rev. B* **2011**, *84* (24), 245301.
(38) Dal Forno, S.; Lischner, J. Electron-Phonon Coupling and Hot Electron Thermalization in Titanium Nitride. *Phys. Rev. Mater.* **2019**, *3* (11), 115203.
(39) Saha, B.; Saber, S.; Naik, G. V.; Boltasseva, A.; Stach, E. A.; Kvam, E. P.; Sands, T. D. Development of Epitaxial Al x Sc 1− x N for Artificially Structured Metal/Semiconductor Superlattice Metamaterials. *Phys. status solidi* **2015**, *252* (2), 251−259.
(40) Rösner, H.; Koch, C. T.; Wilde, G. Strain Mapping along Al−Pb Interfaces. *Acta Mater.* **2010**, *58* (1), 162−172.
(41) Garbrecht, M.; Hultman, L.; Fawey, M. H.; Sands, T. D.; Saha, B. Tailoring of Surface Plasmon Resonances in TiN/(Al0.72Sc0.28)N Multilayers by Dielectric Layer Thickness Variation. *J. Mater. Sci.* **2018**, *53* (6), 4001−4009.
(42) Maurya, K. C.; Shalaev, V. M.; Boltasseva, A.; Saha, B. Reduced Optical Losses in Refractory Plasmonic Titanium Nitride Thin Films Deposited with Molecular Beam Epitaxy. *Opt. Mater. Express* **2020**, *10* (10), 2679.
(43) Herzing, A. A.; Guler, U.; Zhou, X.; Boltasseva, A.; Shalaev, V.; Norris, T. B. Electron Energy Loss Spectroscopy of Plasmon Resonances in Titanium Nitride Thin Films. *Appl. Phys. Lett.* **2016**, *108* (17). DOI: 10.1063/1.4947442.
(44) Pflüger, J.; Fink, J.; Weber, W.; Bohnen, K. P.; Crecelius, G. Dielectric Properties of TiCx, TiNx, VCx, and VNx, from 1.5 to 40 EV Determined by Electron-Energy-Loss Spectroscopy. *Phys. Rev. B* **1984**, *30* (3), 1155−1163.
(45) Rana, A.; Sharma, N. K.; Bera, S.; Yadav, A.; Gupta, G.; Rana, A. S. Tuning the Plasmonic Resonance in TiN Refractory Metal. *Sci. Rep.* **2024**, *14* (1), 7905.
(46) March, N. H.; Paranjape, B. V.; Teshima, R. Plasmon Loss Function Related to Relaxation Time in Metals and Alloys. *Solid State Commun.* **1987**, *63* (8), 757−759.
(47) Paul, A.; Birol, T. Strain Tuning of Plasma Frequency in Vanadate, Niobate, and Molybdate Perovskite Oxides. *Phys. Rev. Mater.* **2019**, *3* (8), No. 085001.
(48) Ben, X.; Park, H. S. Strain Engineering Enhancement of Surface Plasmon Polariton Propagation Lengths for Gold Nanowires. *Appl. Phys. Lett.* **2013**, *102* (4). DOI: 10.1063/1.4790293.
(49) Zhang, S.; Sun, T.-Y.; Wang, Z.; Zhang, R.; Lin, Y.; Xiao, S.; Su, G.; Bi, J.; Li, P.; Zhang, H.; Liang, L.; Yang, F.; Zhang, Q.; Huang, L.-F.; Cao, Y. Engineering Carrier Density and Effective Mass of Plasmonic TiN Films by Tailoring Nitrogen Vacancies. *Nano Lett.* **2024**, *24* (40), 12568−12575.
(50) Catellani, A.; Calzolari, A. Plasmonic Properties of Refractory Titanium Nitride. *Phys. Rev. B* **2017**, *95* (11), 115145.


https://doi.org/10.1021/acs.nanolett.6c01304
*Nano Lett.* 2026, 26, 6482−6489